

Molecular Dynamics Simulations of Turbostratic Dry and Hydrated Montmorillonite with Intercalated Carbon Dioxide

Evgeniy M. Myshakin,^{*,†,‡} Meysam Makaremi,^{†,¶} Vyacheslav N. Romanov,[†]
Kenneth D. Jordan,^{†,¶} and George D. Guthrie[†]

[†]*National Energy Technology Laboratory, 626 Cochrans Mill Road, Pittsburgh,
Pennsylvania 15236, United States*

[‡]*URS Corporation, P.O. Box 618, South Park, Pennsylvania 15129, United States*

[¶]*University of Pittsburgh, Department of Chemistry, Pittsburgh, Pennsylvania 15260,
United States*

E-mail: Evgeniy.Myshakin@netl.doe.gov

Abstract

Molecular dynamics simulations using classical force fields were carried out to study energetic and structural properties of rotationally disordered clay mineral-water-CO₂ systems at pressure and temperature relevant to geological carbon storage. The simulations show that turbostratic stacking of hydrated Na- and Ca-montmorillonite and hydrated montmorillonite with intercalated carbon dioxide is an energetically demanding process accompanied by an increase in the interlayer spacing. On the other hand, rotational disordering of dry or nearly dry smectite systems can be energetically favorable. The distributions of interlayer species are calculated as a function of the rotational angle between adjacent clay layers.

Introduction

Carbon capture and storage technologies offer an important option for reducing CO_2 emissions and mitigating global climate change.¹ The technology of geologic CO_2 storage involves injection of supercritical CO_2 ($scCO_2$) into deep geologic formations overlain by sealing rocks that prevent buoyant CO_2 from migrating upward and out of the storage reservoir. The ability of cap rocks to retain injected CO_2 depends on their ability to maintain low permeability.² Caprocks are often composed of shale or mudstone enriched with swelling clay minerals that may expand or contract upon interaction with $scCO_2$ that, in turn, could impact seal permeability, CO_2 mobility, or both.³⁻⁵ Intercalation of CO_2 into the interlayer of swelling clay can cause geo-mechanical stress and affect the integrity of cap rocks and the ability of geological formations to contain stored CO_2 .⁵⁻⁷ The integrity of the cap rock is important because CO_2 , being more buoyant than saline water and oil, will tend to migrate above these relatively immiscible fluids. Moreover, swelling clay minerals may also provide sites for sorption of CO_2 ^{5,8-11} or environments for its transformation into carbonates.¹²

Swelling clay minerals generally fall into the smectite group, which consists of a group of layered aluminosilicate mineral species with a wide range in compositional variability. We have focused our study specifically on montmorillonite (MMT), for which the central dioctahedral sheet is composed of octahedrally coordinated aluminum (Al) atoms and the adjacent sheets contain tetrahedrally coordinated silicon (Si) atoms. These sheets comprise a 2:1 or tetrahedral-octahedral-tetrahedral (TOT) layer. In MMT, the TOT layers are negatively charged due to substitution of divalent metals (e.g., Mg^{2+} for Al^{3+} in the octahedral sites). The negative charge of the TOT layers is counterbalanced by interlayer cations (e.g., Na^+ , K^+ , Ca^{2+} , etc.) that can exhibit a variety of hydration states, causing expansion or contraction of the interlayer distance of the clay, depending on the relative humidity.¹³ Recent X-ray diffraction (XRD), excess sorption, and neutron diffraction studies showed that the spacing between the mineral layers (basal d-spacing) of Na-rich-MMT expands upon interaction with gaseous CO_2 and $scCO_2$ and that the degree of expansion depends on the initial water content in the

interlayers.^{7,11,14} Those measurements indicated that the largest expansion is accompanied by an increase in the basal d-spacing from 11.3 to 12.3 Å, the number corresponding to a stable monolayer (the 1W hydration state characterized with basal $d_{spacing}$ s in the range of 11.5-12.5 Å; upon incorporation of more water, the d-spacing increases to 14.5-15.5 Å to the stable 2W hydration state where water forms a bilayer structure).^{13,15} Interaction of anhydrous $scCO_2$ with smectite clay in the 2W and higher hydration states may lead in a collapse of the d-spacing to that of the 1W state.^{4,5} However, interaction of Na-exchanged Wyoming montmorillonite (SWy) and Ca-exchanged Texas montmorillonite (STx) samples with variably wet $scCO_2$ (2-100 % saturation of H_2O) induces swelling even to the values equal to the 3W state with a d-spacing of 18.8 Å.^{4,5} Thus, dry $scCO_2$ injected in a target reservoir has the capacity to dehydrate clay and to promote fracturing of cap rocks. On the other hand, after CO_2 becomes saturated by brine, it can induce further swelling of clay. Loring et al.¹⁰ confirmed intercalation of CO_2 by means of NMR spectroscopy and attenuated total reflection infrared spectroscopy. Using diffuse-reflectance infrared spectroscopy, Romanov⁸ reported a red shift of the characteristic fundamental frequency of CO_2 trapped in SWy and STx samples. The source of that shift was attributed to interaction of the intercalated CO_2 molecules with dipoles of water molecules.¹⁶

Botan et al.¹⁷ carried out Monte Carlo (MC) and molecular dynamics (MD) simulations of CO_2 intercalation into Na-MMT using a force field for clay from Smith¹⁸ and the SPC¹⁹ and EPM2²⁰ models for water and carbon dioxide, respectively. In line with experimental data,^{4,5,7,11,14} their simulations showed that hydrated clay intercalates CO_2 and that the thermodynamically stable structures are characterized with basal d-spacings corresponding to the 1W and 2W hydration states. Other modeling studies using different force fields also point out that CO_2 molecules can exist in the interlayers of clay minerals.²¹⁻²⁴ Krishnan et al.²⁴ recently reported information on the molecular-scale structure and dynamics of interlayer species in MMT- CO_2 systems. An excellent review of the recent advances in molecular modeling of CO_2 -brine-mineral interactions is given in ref.²⁵

Another major feature of swelling clay minerals is related to rotational disorder inherently present in natural samples and manifesting itself through turbostratically stacked clay layers.^{26–29} Turbostratic disorder, a disorder in which different layers have different rotations with respect to an axis, is commonly found in naturally occurring samples of montmorillonite.^{28,29} To reconcile apparent discrepancies between high resolution transmission electron microscopy (HRTEM) images and powder X-ray diffraction (XRD),^{30,31} Guthrie and Reynolds¹⁶ offered a model in which adjacent TOT layers of smectite are turbostratically stacked within $\sim 2–10$ degree rotation of each other.^{30–33} In this model, rotation of adjacent TOT layers results in breaking of coherency between the ditrigonal rings in the silica sheets on either side of the interlayer, thereby changing the framework structure that bounds the interlayer region. Instead of having a coherent alignment of ditrigonal rings on either side of the interlayer region, rotational disorder results in a Moire pattern with a periodic variation in alignment of ditrigonal rings across the interlayer. In the simulations, smectite models are assumed to be perfectly oriented, and any impacts of rotational disorder are generally ignored. However, understanding interactions between interlayer species and rotationally disordered clay systems is mandatory to properly predict the behavior of geological formations and cap rocks under carbon dioxide invasion. In the present study, classical molecular dynamics simulations are used to investigate the process of rotational disordering in MMT at various water and carbon dioxide contents. The simulations were carried out at P-T conditions relevant to geological formations for CO_2 storage. The main focus of the study is placed on comparison of energetic and structural changes associated with deviation of the clay layers from their ideally stacked positions. In addition, one-dimensional density profiles and two-dimensional density maps are engaged to study the distributions of interlayer species as a function of the rotational angle between adjacent TOT layers.

Computational Details

Classical Force Field Simulations

The force field calculations were carried out using the GROMACS package.³⁴ For the clay system, the Clayff force field³⁵ that consists of nonbonded (electrostatic and van der Waals) terms parametrized for use with layered minerals was employed. For atoms i and j separated by a distance r_{ij} , the pairwise energy is given by

$$E_{ij} = \frac{q_i q_j e^2}{4\pi\epsilon_0 r_{ij}} + 4\epsilon_{ij} \left[\left(\frac{\sigma_{ij}}{r_{ij}} \right)^{12} - \left(\frac{\sigma_{ij}}{r_{ij}} \right)^6 \right] \quad (1)$$

where q_i is the charge on atom i , ϵ_0 is the vacuum permittivity, and ϵ_{ij} and σ_{ij} are the Lennard-Jones (LJ) energy and distance parameters, respectively. The flexible SPC model¹⁹ was used for the water molecules placed in the interlayer space and for the layer hydroxyl groups. For CO_2 , a recently developed flexible potential including intramolecular bond stretch and angle bend was used.³⁶ The general expression for the total potential energy is

$$E_{total} = E_{Coul} + E_{Vdw} + E_{stretch} + E_{bend} \quad (2)$$

where harmonic potentials are used for the bond stretch and angle bend terms.

The Lorentz Berthelot mixing rule³⁷ was used to obtain the LJ parameters for interactions between unlike atoms. It is worth mentioning that in an earlier paper¹⁶ we showed that the description of CO_2 in liquid water using the force fields described above closely reproduces that obtained with simulations using "polarization-corrected" LJ parameters for the unlike pair interactions in water/carbon dioxide mixtures.³⁸ The authors of ref³⁸ used the SPC/E and EPM2 force fields to simulate CO_2 in liquid water and to accurately reproduce the experimental solubilities.

In the present study, the simulations were performed under periodic boundary conditions (PBC) and used the particle- particle particle-mesh (PPPM) Ewald method to treat long

range electrostatics.³⁷ The cutoff radii for the nonbonded van der Waals interactions and for the Ewald summation of the electrostatics were chosen to be 11 Å, with switching distances starting from 10 Å. Because of the use of cutoffs for the LJ interactions, long-range dispersion corrections for energy and pressure were applied.³⁴ The leapfrog algorithm³⁹ was used to update positions every 0.5 fs.

Simulations of the turbostratically disordered clay layers is not a trivial task. Rotation of one clay layer relative to another destroys the periodicity of the systems which is problematic in simulations using PBC. To preserve periodicity, the clay systems represent a rectangular box with uneven sizes of alternating clay layers (designated as "small" and "large"). Thus, within a chosen angular range, rotation of small layers proceeds within the boundaries of the simulation box defined by large ones. This approach allows us to use PBC and to provide external clay surfaces (clay edges) and the interstitial space between the alternating layers accessible to the interlayer species. The interstitial space is produced because of gaps between adjacent replicas of small layers. In turbostratic clay systems, the clay layers are stacked in the z direction, so the rotation of a small layer relative to a large one occurs in the xy plane around the axis connecting geometrical centers of the layers and perpendicular to the internal clay surfaces. The [100] and [010] edges introduced by the presence of the small layers are determined by the structure of the unit cell. Because the Clayff force field³⁵ contains no bonding terms except for the hydroxyl groups, there are no broken chemical bonds at the edges.

The general chemical formula used for sodium montmorillonite is $Na_xMg_xAl_{3-x}Si_4O_{10}(OH)_2nH_2O$, where the layer charge resides on the octahedral sheet (tetrahedral substitutions such as Al^{3+} for Si^{4+} can also occur in natural samples but they are not considered here). In addition to sodium ions, calcium and potassium (dry clay systems only) ions were also used as interlayer ions in the simulation models. The MMT structural model was created by replicating a pyrophyllite unit cell with an isomorphic octahedral Al^{3+}/Mg^{2+} substitution to produce a rectangular $22 \times 14 \times 1(18 \times 10 \times 1)$ supercell, in which the first set of numbers

designates the size of the large layer and the second one (in parentheses) designates the size of the smaller layer. The initial dimensions of the simulation box in the x and y directions were 114.4 and 128.8 Å, respectively. The dimension in the z direction varies depending on the interlayer composition. The negative charge introduced by the substitutions is compensated by 366 sodium ions (or 183 calcium ions) residing in the interlayers.

The stoichiometry is $Na_{0.75}Mg_{0.75}Al_{3.25}(OH)_4(Si_4O_{10})_2$, with a layer charge of 0.75 per $O_{20}(OH)_4$. This results in a total of 19520 atoms constituting the clay phase. Additional simulations were performed for the dehydrated systems using a simulation box doubled in size in the z direction to ensure that there is no size effect on the results of simulations. In these tests, the systems are described with a $22 \times 14 \times 2(18 \times 10 \times 2)$ supercell. In addition, a $22 \times 12 \times 2(18 \times 10 \times 2)$ supercell was used to confirm independence of reported below results on the size of the interstitial space. MD simulations using a $8 \times 4 \times 4$ supercell were also carried out for dehydrated MMT systems to estimate equilibrium d_{001} -spacing values for clay systems providing exposure of the ions to internal surfaces only (i.e., without edges). The water/ CO_2 composition in the interlayer region is designated as X-Y, where X and Y are, respectively, the numbers of water and CO_2 molecules per unit cell. There are four types of interlayer compositions used in the simulations: the first one (0-0) contains only interlayer ions without water and represents the dehydrated clay phase; the second (X-0) contains X water molecules per unit cell; the third (0-Y) includes Y carbon dioxide molecules per unit cell only, and the fourth (X-Y) contains both X water and Y CO_2 molecules per unit cell. The maximum number of atoms engaged in the simulations was 40214 in the case of the clay system (Na- MMT with a $22 \times 14 \times 2(18 \times 10 \times 2)$ supercell) with the 14-0 composition. The initial positions of the ions, water, and carbon dioxide molecules were chosen randomly in a plane at the middle of the interlayers. They are placed nearly equidistantly from each other, and the plane dimensions are equal to the x and y dimensions of the large layer. For the dry, CO_2 only, and hydrated clay systems, multiple independent simulations starting from different initial structures were performed to ensure that the computed trends were

consistent and were not affected by different initial positions. Because of the gaps between small layers, direct comparison of the energetic and structural parameters with those computed for systems without explicit presence of edges is not straightforward. Particularly, the numbers of water molecules per unit cell corresponding to the d_{001} -spacings at the stable hydration states (1W, 2W, etc.)^{24,36} are not the same for the systems considered in this work because water molecules reside in both the interlayer and the interstitial space. For the X-Y compositions, the concentrations of CO_2 and H_2O in the interlayer and the interstitial space could vary and depend on the initial positions of the species. However, regardless of that, the relative energetic and d_{001} -spacing trends as a function of the rotational angle (θ) remain the same. For the X-Y compositions, the results are reported using the initial distribution of the species similar to that described above.

MMT with intercalated species was initially relaxed using MD simulations in the NVT ensemble carried out for 50 ps at $T = 348.15$ K. Subsequent equilibration was conducted for 1 ns using the NPT ensemble with the weak coupling Berendsen thermostat and barostat⁴⁰ at $T = 348.15$ K and $P = 130$ bar, conditions close to those existing in subsurface geological reservoirs and cap rocks and also close to those used in CO_2 intercalation experiments in clays carried out at National Energy Technology Laboratory (NETL).⁸ That step was followed by 20 ns production runs in the NPT ensemble at the same P-T conditions with semi-isotropic pressure coupling permitting the z-dimension to fluctuate independently from the x and y directions. Pressure was controlled by a Parrinello-Rahman barostat^{41,42} with a relaxation time of 4 ps, and the temperature was controlled by a Nose-Hoover thermostat^{43,44} with a relaxation time of 2 ps. The analysis of different terms contributing to the net potential energy was performed using the equilibrated clay structures. For that purpose, MD simulations were performed over 300 ps in the NVT ensemble using a Nose-Hoover thermostat^{43,44} with a relaxation time of 2 ps.

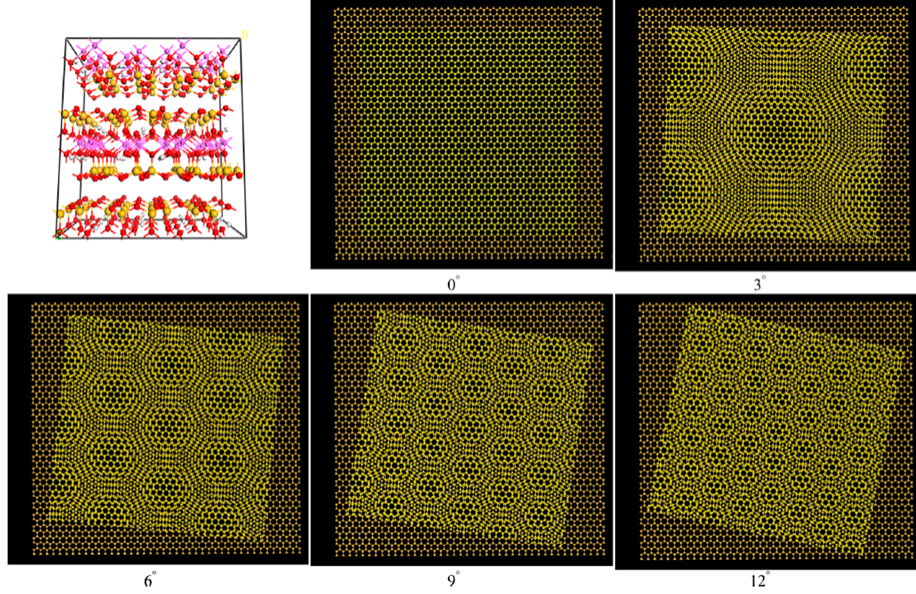


Figure 1: The [100] edge face of the 2:1 smectite clay structure (pyrophyllite) and Moiré patterns formed by two adjacent basal surfaces at 0-12° (from the [001] view). Color designation: red balls, oxygen; yellow, silicon; white, hydrogen; cyan, aluminum.

Rotational Pattern Model

Figure 1 shows a schematic diagram of two adjacent tetrahedral sheets formed by basal oxygens and silicon atoms starting from perfectly juxtaposed sheets and with rotation angles of 3, 6, 9, and 12° together with the 3D smectite structure (pyrophyllite was taken for simplicity with the expanded size of the sheets to fully capture the pattern at $\theta = 3^\circ$). For perfectly aligned sheets, two ditrigonal rings of silicon tetrahedra linked by shared basal oxygens locate above each other and create a cavity shown in Figure 2a. Rotational mismatch results in complex cavities reflecting a variation in alignment of the ditrigonal rings across adjacent clay sheets. The variation in cavity structure is periodic, forming a Moiré pattern with concentric circles of partially aligned ditrigonal rings separated by regions of no alignment (Figures 1 and 2b). For small rotational shifts, the distances between the centers of the circles along a layer are given by

$$d_{MP} = \frac{d_a}{2\sin(\frac{\theta}{2})} \quad (3)$$

where d_{MP} is the distance between centers of two circles in the Moire pattern, d_a is the distance between centers of ditrigonal rings of the same layer and equal to the a lattice, and θ is the angle by which one layer is rotated relative to another. Assuming a d_a value equal to 5.20 /AA (a typical distance for the a lattice constant of MMT⁴⁵) the calculated d_{MP} values are 99, 50, 33, and 25 Å for $\theta = 3^\circ, 6^\circ, 9^\circ,$ and 12° , respectively. Those numbers dictate that to capture the patterns, a sufficiently large model is required. To fulfill this requirement, the size of the simulation box was chosen as described in section 2.1. The area of one unit cell (Figure 2b; inside the blue arrows) formed by the rotational pattern is further determined as

$$S_{MP} = d_{MP}^2 \sin(\pi/3) = \frac{\sqrt{3}}{2} \frac{d_a^2}{(2\sin(\frac{\theta}{2}))^2} \quad (4)$$

The area of the concentric circle itself is computed as

$$S_{IS} = \pi d_{IS}^2 = \frac{\pi d_a^2}{(2F\sin(\frac{\theta}{2}))^2} \quad (5)$$

where d_{IS} is the radius within which the shifted ditrigonal rings are still viewed as forming concentric circles, θ has the same meaning as in eq 3, and F is a factor determining the fraction of the unit cell that belongs to the circles. This formula is valid until d_{IS} is larger than the lattice parameter a . Assuming that the concentric circles occupy 1/3 of the unit cell area, the limiting value of the θ angle is 17.4° , after which the rotational pattern disappears. Thus, the chosen range of the rotational angles, $[0-12^\circ]$, passes through the various Moire patterns and reflects the interval of angles consistent with TEM observations²⁹⁻³² Another implication of this model is that the ratio of the unit cell area to the concentric circle area does not depend on θ . This means that the fraction of the concentric circles remains fixed during the limited range of rotation considered. From the mathematical model presented above, it follows that the number of cavities formed by basal oxygens of the adjacent layers (Figure 2a) is constant within the rotation range, although their distribution is varied. By definition, that number is smaller than the number of (undistorted) cavities for the 0° case,

in which clay layers are perfectly aligned.

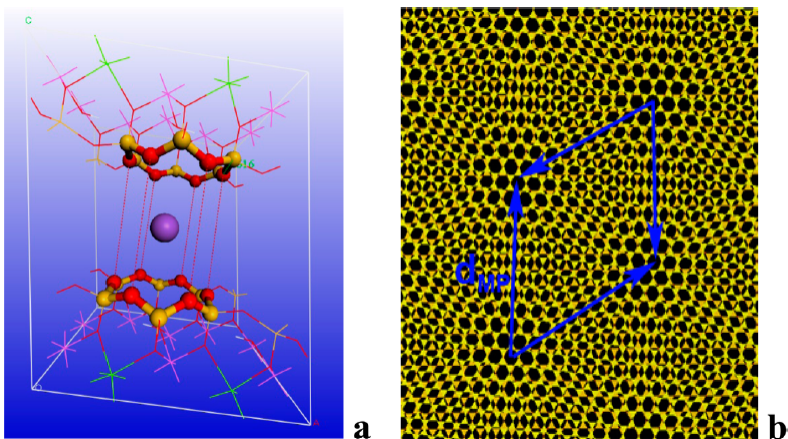


Figure 2: (a) A "cavity" formed by basal atoms of adjacent clay layers and (b) the unit cell of the Moire pattern.

Methods To Study Rotational Disordering

The question of the time scales of rotational motion of clay layers is most intriguing. On one hand, the clay minerals in a geological formation could be exposed to geo-mechanical stress for decades, which essentially implies nearly equilibrium conditions for interlayer species during rotation. On the other hand, local perturbations of a subsurface geological reservoir due to CO_2 injection could create mechanical forces acting on clay-rich deposits to impose rotational motion of the layers at non-equilibrium conditions. Hence, our simulation approaches stem from the intention to simulate both rotational disordering occurring on geological time scales and during injection of a mobile phase into porous media of target formations. The method mimicking geological conditions deals with rotated clay systems with predetermined θ angles, at which interlayer species are equilibrated. The second method rotates alternating clay layers around a fixed axis with a constant angular velocity. Details of the two methods are given below.

Position Restraining

In this approach, the rotationally disordered and 0° systems were initially prepared as described in section 2.1. The clay systems were equilibrated at $\theta = 0^\circ, 3^\circ, 6^\circ, 9^\circ,$ and 12° . The production runs with various compositions of the interlayer species were carried out using the procedure described above. To keep the atomic positions of the clay phase at the predetermined angles, the atoms were harmonically restrained in the XY plane at their reference positions using a force constant of 5000 kJ/mol.nm². This approach provides no translational motion of the clay layers relative to each other. Those degrees of freedom might be important for equilibration.⁴⁶ The Z coordinates remained unconstrained, allowing the simulation box to adjust its dimension in that direction during the simulations. This approach provides equilibration of interlayer species in the turbostratic clay systems (monitored using constancy of potential energies and d_{001} -spacings over simulation time) at the rotational angles of interest.

Enforced Rotation

Various methods for enforcing the rotation of subsets of atoms have been reported by Kutzner et al.⁴⁷ In the approach engaged in this work, a force is imposed on the group of atoms constituting the small clay layer by means of rotating a reference set of atomic positions, y_i^0 (coinciding with initial atomic positions of the small clay layer), at a constant angular velocity, ω , around a fixed axis defined through a geometrical center of the clay layer and that is perpendicular to the clay surfaces. The rotation is performed in such a manner that each atom with position x_i is connected by a "virtual spring" represented by a harmonic potential to its moving reference position: $y_i = \Omega(t)(y_i^0 - y_c^0)$, where $\Omega(t)$ given below is a dimensionless matrix describing the rotation around the axis, t is time, and y_c^0 is the geometrical center of the initial reference positions (in this case, it corresponds to the geometrical center of the

small clay layer).

$$\begin{pmatrix} \cos\omega t + \nu_x^2\xi & \nu_x\nu_y\xi - \nu_z\sin\omega t & \nu_x\nu_z\xi + \nu_y\sin\omega t \\ \nu_x\nu_y\xi + \nu_z\sin\omega t & \cos\omega t + \nu_y^2\xi & \nu_x\nu_z\xi - \nu_x\sin\omega t \\ \nu_x\nu_z\xi - \nu_y\sin\omega t & \nu_x\nu_z\xi + \nu_x\sin\omega t & \cos\omega t + \nu_z^2\xi \end{pmatrix} \quad (6)$$

where ν_x , ν_y , and ν_z are the components of the normalized rotation vector, ν and $\xi = 1 - \cos\omega t$. To achieve unrestrained motion along the rotational axis and to allow adjustment of the d_{001} -spacing during rotation, the components of the potential parallel to the axis are removed. This is done by projecting the distance vectors between the reference and actual atomic positions onto the plane perpendicular to the rotation axis. Thus, the final form of the potential is

$$V^{rot} = \frac{k}{2} \sum_{i=1}^N \Omega(t)(y_i^0 - y_c^0) - (x_i - x_c) - \Omega(t)(y_i^0 - y_i^0) - (x_i - x_c)\nu\nu^2 \quad (7)$$

where k is a spring constant and x_c is the geometrical center of the group (the small clay layer), and x_i , y_i^0 , y_c^0 , ν , ω , and t are defined above. The details of the implementation can be found elsewhere.⁴⁶ The k value was chosen to be 100 kJ/mol.nm², which is low enough to ensure smooth transitions between atomic positions. To perform the enforced rotation, the clay systems were first equilibrated at various compositions of the interlayer species at $\theta = 0^\circ$. Rotation was induced around the axis at an angular rate of $\omega = 0.01^\circ/\text{ps}$ over 1.2 ns with a step size of 0.5 fs. This produces a 12° rotation of the clay layers passing various Moire patterns. Additional simulations were conducted using $\omega = 0.001^\circ/\text{ps}$ to study the dependence of potential energy on the angular rate.

Results and Discussion

Table 1 compares the d_{001} -spacings of dry M-MMT (M = metal ion) computed in this work with those from DFT calculations

Table 1: d_{001} -Spacing Parameters for Dry M-MMT Systems

ion	this work	DFT(vdW-TS)	exptl
Na^+	9.52 ± 0.02 ; (9.43 ± 0.01)	9.47^b	9.6^c ; 9.6^d
Ca^{2+}	9.56 ± 0.02 ; (9.42 ± 0.01)	9.33^b	10.0^c ; 9.6^d
K^+	10.24 ± 0.03 ; (9.83 ± 0.02)	9.88^b	10.0^c ; 10.0^d ; 10.2^e

^a The values in parentheses are computed using a $8 \times 4 \times 4$ supercell. ^bRef. ⁴⁷ ^cRef. ⁴⁸
^dRef. ⁴⁹ ^eRef. ⁵⁰

with dispersion corrections⁴⁷ and from experiment as inferred from the relative proportions

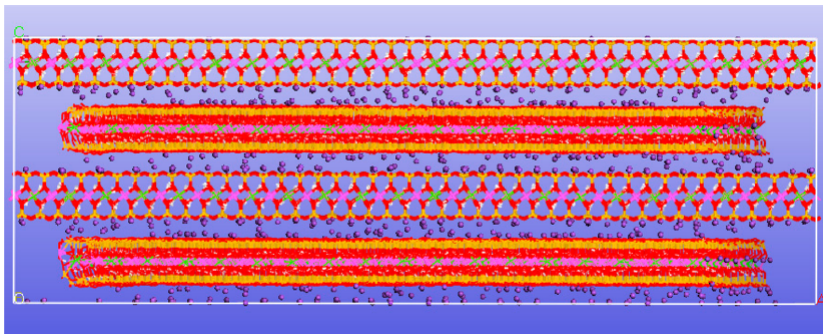


Figure 3: Equilibrium structure of the dehydrated Na-MMT system at $\theta = 6^\circ$. Color designation: red balls, oxygen; yellow, silicon; cyan, aluminum; green, magnesium; purple, sodium ion; white, hydrogen.

of the different layer types as a function of relative humidity.^{48–50} There is an overall good agreement between the computed and measured data, although the experimental d_{001} -spacing values are prone to large uncertainties because the experimental samples were prepared by dehydrating humidity-exposed clays, which may have caused the original structure not to be preserved.^{51,52} Figure 3 depicts equilibrated structures of dry Na-MMT at $\theta = 6^\circ$ (as an example). The disordering is represented as alternating clay layers rotated around an axis perpendicular to the internal clay surfaces. In a previous paper¹⁶ using the same force fields,^{35,36} we demonstrated that the expansion of the d_{001} -spacing of Na-MMT upon

intercalation of water closely reproduces the experimental dependence of the d_{001} -spacing as a function of interlayer water content.¹³ The d_{001} -spacing displays plateaux corresponding to a stable hydration states.¹³ The predicted d_{001} -spacings are also consistent with recently reported data on Na-montmorillonite and Na-hectorite.^{24,36,53}

Figures 4 and 5 display, respectively, the relative changes in the potential energy and the d_{001} -spacing as a function of X-Y interlayer compositions and the θ angle. These data were obtained using atomic positions constrained to predetermined θ angles. The upper part of each figure shows data without carbon dioxide, and the lower part reports results with intercalated CO_2 . The interlayer spacing changes within a narrow 0.2 Å range (except the Ca-MMT system at the 5.2 composition, which displays a variation of up to 0.35 Å) upon rotation. The differences between the calculated enthalpy and potential energy changes are negligible, so in the subsequent analysis, we use the potential energy as the quantity to analyze energy dependencies.

In general, the largest changes in the potential energy and structural parameters occur during rotation from 0° to 3° , and a further increase in θ perturbs the systems to a lesser extent(except for the 0.2 composition). This might be related to the fact that the ratio of the unit cell area to the concentric circle area does not depend on θ (see Computational Details). Consequently, the numbers of distorted and undistorted cavities remain fixed. Introduction of Ca^{2+} and K^+ counterions produce more noticeable changes in the energy and interlayer distance than found for the Na^+ ion. Thus, cations having larger ionic radii and charge affect the potential energy and the interlayer distance more. Below, we consider the dehydrated, hydrated, and clay systems with intercalated carbon dioxide separately, paying attention to the energetic and structural changes and the density distributions of the interlayer species as a function of θ .

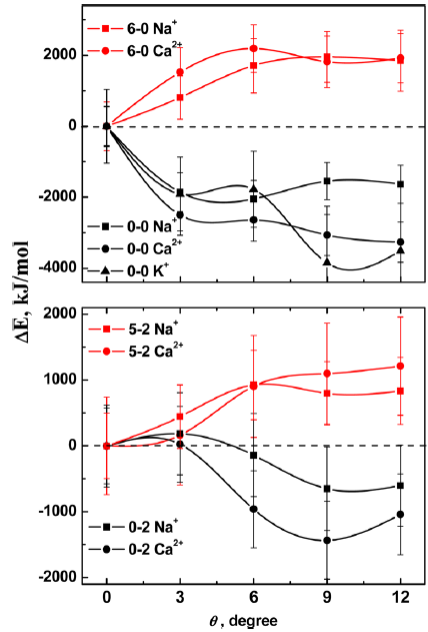


Figure 4: Relative potential energy change in M-MMT systems as a function of interlayer compositions and θ .

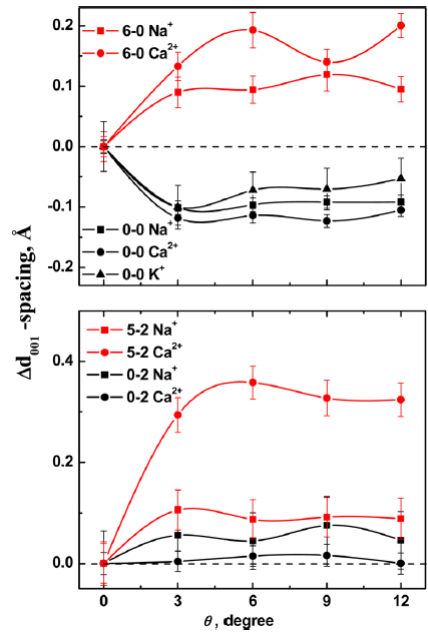


Figure 5: Relative d_{001} -spacing change in M-MMT systems as a function of interlayer compositions and θ .

Rotation of Dry Clay Systems

For the dehydrated clay systems, the potential energies for the twisted structures are lower than for the structure at $\theta = 0^\circ$ (Figure 4). The corresponding d_{001} -spacings also demon-

strate decreased values compared with the $\theta = 0^\circ$ case (Figure 5). The figures depict the intriguing result that the energy and the d_{001} -spacing are lower for the rotated dehydrated Na- and Ca-MMT systems than for the clay structures at $\theta = 0^\circ$. The ions can be coordinated equidistantly to negatively charged basal oxygens of ditrigonal rings in perfectly juxtaposed clay sheets (Figure 2a). Such coordination provides optimal interaction, resulting in lowering of total energy. Because rotation causes reduction in a number of those cavities, as evidenced by the formation of the Moire patterns (Figure 1), the total energy of the system would have been expected to increase. Before addressing this issue, it is important to mention that the dry clay systems considered in this study are idealized structures. In reality, a smectite sample in the 0W hydration state is expected to have residual water bound to interlayer ions.⁴⁸ To check the effect of trace amounts of water on the potential energy and interlayer distance, a set of simulations using 0.25 water molecule per unit cell of Na-MMT was conducted. These simulations gave energies and d_{001} -spacings of rotated structures at $\theta > 0^\circ$ lower than the corresponding values at $\theta = 0^\circ$. Thus, even with a small amount of water present, the distribution of interlayer ions still controls the trends in relative energy and d_{001} -spacing depicted in Figures 4 and 5. We now turn to the results for the fully dehydrated Na- and Ca-MMT systems.

The atomic density profiles for the 0.0 composition depicted in Figure 6a indicate that Na^+ ions (and Ca^{2+} , not shown) display two asymmetric peaks located near the basal planes designated by the dashed lines. The asymmetry is caused by different sizes of the alternating clay layers, as described in Computational Details. This trend does not depend on the initial positions of the ions. The analysis of the distances between the ions and the basal oxygens shows that ions associated with the density peaks are preferentially coordinated at the middle of the ditrigonal rings within 2.9 Å (estimated for sodium ions) from three and more basal oxygen atoms, thus meeting the criterion used to assign an ion as adsorbed.¹⁶ This coordination does not depend on initial positions and is reproduced with independent

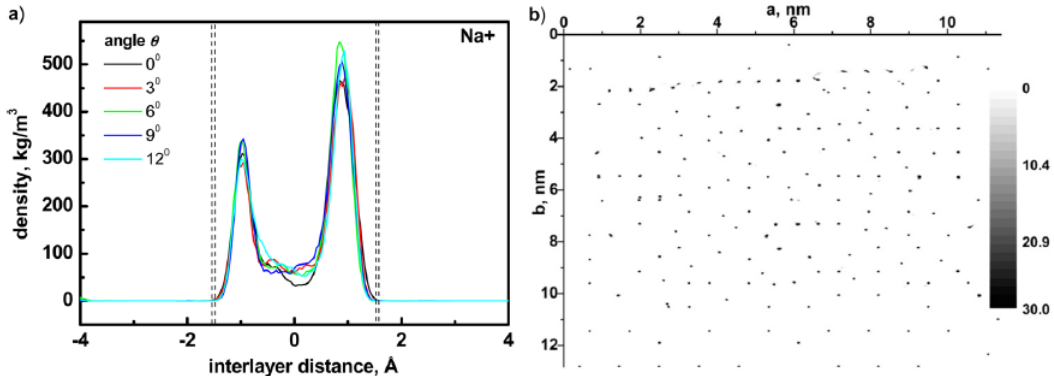


Figure 6: (a) Density profiles showing sodium ion distribution along the distance perpendicular to the internal surfaces of Na-MMT with the 0-0 composition at various values. Double dashed lines designate the range of positions of basal planes as a result of rotation. Profiles obtained by averaging over 5 ns of simulation time. (b) Density map (density in number/nm³) showing the sodium ion distribution in the interlayer projected on a plane parallel to the internal surfaces of Na-MMT with the 0-0 composition at $\theta = 6^\circ$. Results obtained by averaging over 5 ns of simulation time.

simulations. Morrow et al.⁵³ also found that in dehydrated samples of Na-hectorite, the Na^+ ions lie at the center of the hexagonal rings on the sheet to which they are closest. Similar observation was made in the MD simulations of Na-rectorate.⁵⁴ The number of ions is 0.75 (two times smaller in the case of Ca-MMT) per four ditrigonal rings (two on each surface) in a unit cell so that there is no competition for a coordination place that would otherwise force them to stay close to the interlayer center plane. At the middle of the ditrigonal rings, the counterbalancing ions are strongly electrostatically bound to surrounding basal oxygens. The equilibration step allows the interlayer ions to find their energetically favorable configurations at each θ value considered. Such a process might mimic the situation occurring during dehydration of clay samples upon heating. Thus, under (geo)mechanical stress, the interlayer ions in smectite clay minerals slowly losing water would have sufficient time to adjust their positions and promote rotational disordering at least within the range of θ values considered in this work.

Figure 6b depicts the two-dimensional density map for the sodium ions in the interlayer. The map was obtained by scanning the interlayer space to obtain density distributions in

planes parallel to the clay surfaces with a step size of 0.1 Å. Then the distributions were projected on a plane and averaged for 5 ns of simulation time. The map shows that the sodium ions are localized with respect to their XY coordinates (similar distributions were obtained for the other θ angles). This, together with the density profile data, also confirms ion localization near the surfaces.

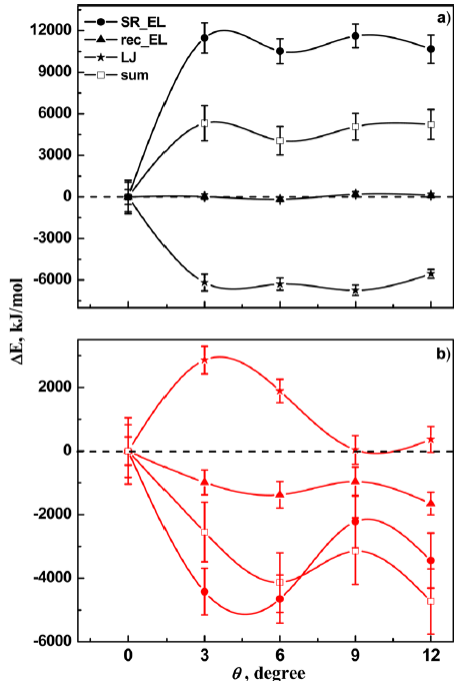


Figure 7: Comparison of real-space electrostatic (SR_EL), reciprocal electrostatic (rec_EL), Lennard-Jones (LJ) contributions and their total sum (sum) as a function of θ for the (a) 6-0 and (b) 0-0 compositions of Ca-MMT.

To gain insight into the interactions responsible for the computed energy trend, contributions from the various terms in the force field were extracted and analyzed. Figure 7 reports short-range (real-space sum accounting for pairwise interactions within a sphere of 11 Å, the cutoff radius), reciprocal space electrostatics and LJ contributions into the relative potential energies as a function of θ for the 6-0 (upper part) and 0-0 (lower part) compositions. The "position-restraining" and "long-range dispersion correction" (a minor modification to the

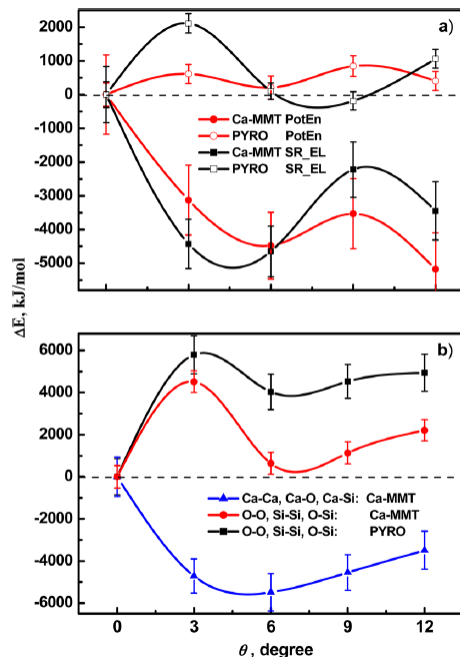


Figure 8: Comparison of (a) relative potential energies (PotEn) and real-space electrostatic contributions (SR_EL) and (b) atomic pairwise electrostatic contributions to relative potential energies in dry Ca- MMT and pyrophyllite with the 0-0 composition at various θ values.

Lennard-Jones terms to remove the noise caused by cutoff effects) terms provide insignificant contributions to the relative potential energies at different θ values (it should be mentioned that the weighted histogram analysis method³⁴ would be valuable for removing the bias due to the restraint and for estimating free energies as a function of θ , but it requires a special effort to be applied for these clay systems and was not considered in this work). For the hydrated system, rotation of the small layer relative to the large one leads to a large electrostatic destabilization, whereas the LJ contribution is energetically favorable. On the other hand, for the dehydrated system, the electrostatics favors the rotated structures with the LJ contribution being positive. Comparing the relative influence of the different terms in the force field, it is seen that short range electrostatic contributions are the most important for the overall potential energy change as a function of θ for both hydrated and dry MMT systems.

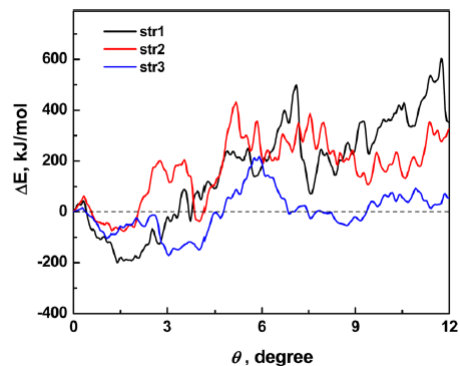


Figure 9: Potential energy changes during enforced rotation for three independently equilibrated Na-MMT systems (strs 1-3) with the 0-0 composition.

To estimate the role of electrostatic contributions involving interlayer ions, simulations were also carried out for pyrophyllite, which does not have octahedral and tetrahedral substitutions in TOT clay layers and, thus, bears neutral layers without interlayer ions. Figure 8 (upper part) depicts the relative potential energies and the relative real-space electrostatic contributions for pyrophyllite and Ca-MMT. The key atomic pairwise electrostatic contributions involving the ions and atoms of basal surfaces are depicted in the lower part of Figure 8. In contrast to Ca-MMT, the rotation of dry pyrophyllite is an energetically demanding process, and for both minerals, the electrostatic contribution to the relative potential energies determines the overall decrease/increase in the potential energies with rotation. The atomic pairwise contributions from the basal oxygen and silicon atoms provide a similar destabilizing impact for the rotated pyrophyllite and Ca-MMT systems. However, in the case of Ca-MMT, the electrostatic contribution involving interlayer ions induces a large stabilization upon rotation. Therefore, the overall decrease of the potential energy of nonhydrated MMT systems with rotation is primarily caused by interactions of interlayer ions with atoms of the clay surfaces.

We now turn our attention to exploring the energetic and structural changes during rotational motion of the small clay layer at a constant angular velocity using the enforced rotation approach. Figure 9 depicts the evolution of the potential energy as a function of θ . Three

independently equilibrated Na-MMT systems with the 0-0 composition at $\theta = 0^\circ$ were used as starting points to initiate simulations, allowing for rotational movement of the small layer relative to the large one. The initial motion from $\theta = 0^\circ$ to $\theta = 0.1-0.2^\circ$ requires overcoming a potential barrier of around 25.50 kJ/mol. The barrier is associated with a deviation of the system from its equilibrium while the Moire pattern is not yet developed (for the size of the clay system employed). After that, as soon as the Moire pattern begins to form, further rotation leads to a decrease in the energy (and in the d_{001} -spacing, not shown) up to $\theta = 1.5-2^\circ$. The energy (and d_{001} -spacing) then increases upon further increase in θ (Figure 9). Analysis of the distribution of the interlayer ions during the enforced rotation shows that the rotational motion does not induce rearrangement of the ions adsorbed at the centers of ditrigonal rings. The energy decreases for $\theta = 0.2 - 2^\circ$ because the ions remain close to equilibrated positions at $\theta = 0^\circ$. However, rotation to larger angles ($> 3^\circ$) causes more unfavorable ion-ion interactions between ions adsorbed at the opposite internal clay surfaces. Those interactions counterbalance the energy decrease that would otherwise result because of rotation. As a result, further disordering beyond $2-3^\circ$ would be significantly retarded.

The simulated rotational motion models the disordering occurring in dehydrated or nearly dehydrated smectite minerals. The energy trends obtained using the enforced rotation are different from those found with the position constraints. The differences originate from the fact that the latter approach allows relaxation of the ion positions at fixed rotational angles, whereas in the former, the ions remain adsorbed at positions corresponding to $\theta = 0^\circ$. The rate of the motion, which is limited by computational cost, is apparently much greater than that occurring in nature and proceeds under nonequilibrium conditions. To explore rotational motion at a reduced angular speed, simulations were performed using a rotational velocity of $0.001^\circ/\text{ps}$. The predicted trends in energy and d_{001} -spacing remain similar to those discussed above. This implies that under mechanical stress, nearly dry smectite clay minerals would be susceptible to rotational disordering within the narrow θ range.

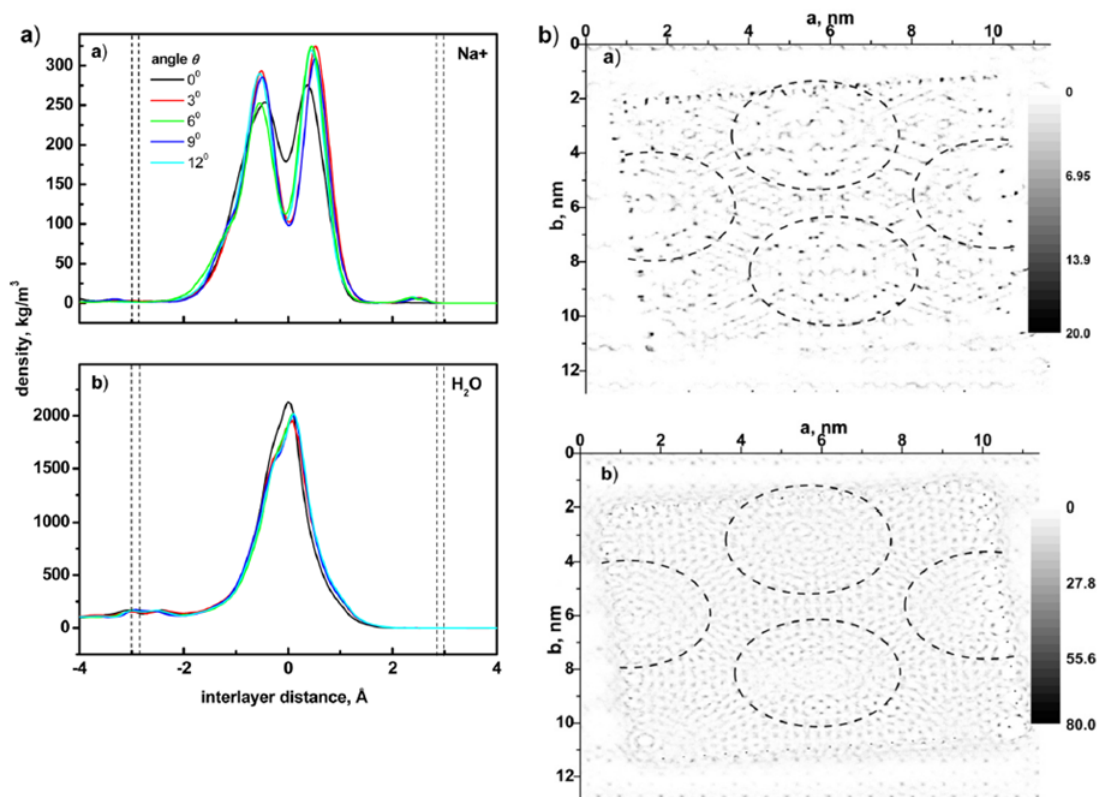


Figure 10: (a; left) Density profiles showing (a) sodium ion and (b) water molecule distributions along the distance perpendicular to the internal surfaces of Na-MMT with the 6-0 composition at various θ . Double dashed lines designate the range of positions of basal planes as a result of rotation. Profiles obtained by averaging over 5 ns of simulation time. (b; right) Density maps (density in number/nm³) showing (a) sodium ion and (b) water molecule distributions in the interlayer projected on a plane parallel to the internal surfaces of Na-MMT with the 6-0 composition at $\theta = 6^\circ$. Results obtained by averaging over 5 ns of simulation time. The Moiré pattern is highlighted with dotted circles.

To explore an effect of the Moiré patterns on the potential energy of dry smectites, simulations with backward enforced rotation of MMT systems were carried out for clay structures at nonzero θ values. Figure S1 (Supporting Information) collects potential energy curves computed during backward rotation for Na-MMT structures with interlayer ions equilibrated using the position restraining method at $\theta = 3^\circ$, 6° , and 9° . The curves develop distinct peaks when rotation of the small layers passes the position of perfectly juxtaposed clay layers at $\theta = 0^\circ$. The deviation from that position in both clockwise and counterclockwise directions leads

to a decrease in energy. Thus, formation of the rotational patterns of adjacent clay surfaces induces a decrease in the potential energy (and d_{001} -spacing) of the dehydrated smectites.

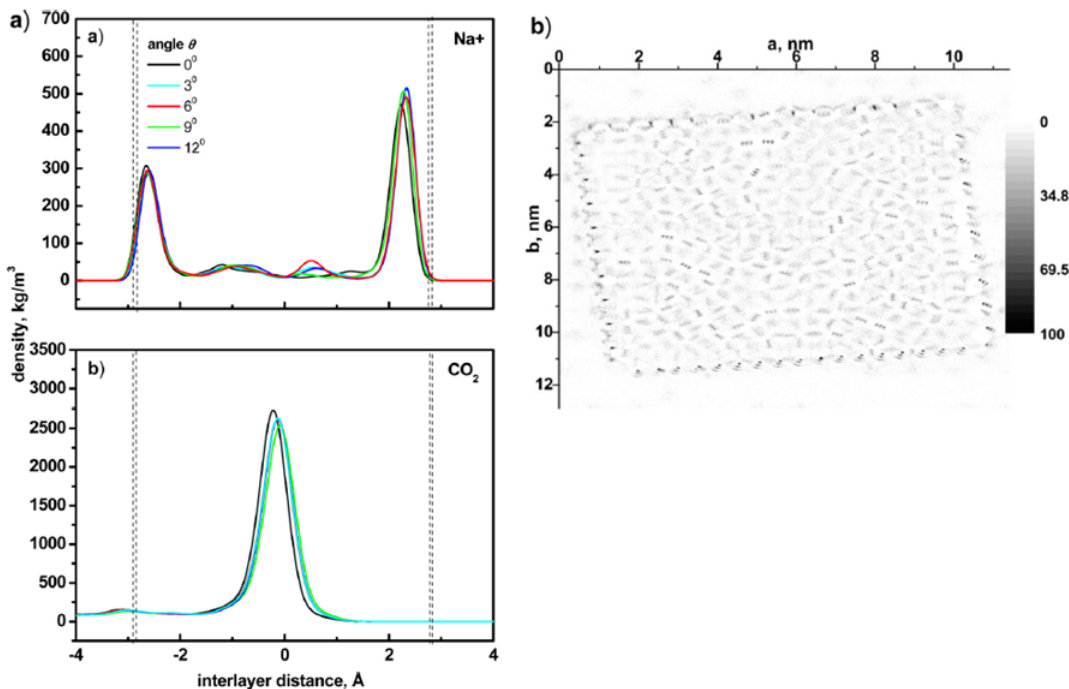


Figure 11: (a; left) Density profiles showing (a) sodium ion and (b) carbon dioxide molecule distributions along the distance perpendicular to the internal surfaces of Na-MMT with the 0-2 composition at various θ values. Double dashed lines designate the range of positions of basal planes as a result of rotation. Profiles obtained by averaging over 5 ns of simulation time. (b; right) Density maps (density in number/nm³) showing carbon dioxide molecule distributions in the interlayer projected on a plane parallel to the internal surfaces of Na-MMT with the 0-2 composition at $\theta = 6^\circ$. Results obtained by averaging over 5 ns of simulation time.

Rotation of Hydrated Clay Systems

According to Figures 4 and 5, rotation of the clay layers of hydrated Na- and Ca-MMT requires energy and is accompanied by expansion of the interlayer distance. The overall trends

in energies, d_{001} -spacings, atomic density distributions, and radial distribution functions are similar for the 2-0, 4-0, 6-0, and 8-0 compositions. We now examine in more detail the results of the simulations for the 6-0 composition, which provides a water monolayer and a d_{001} -spacing equal to $12.10 \pm 0.03 \text{ \AA}$ ($\theta = 0^\circ$). That equilibrated spacing falls within the experimentally determined range of the 1W hydration state ($11.5\text{-}12.5 \text{ \AA}$)¹³ and corresponds to the calculated stable hydration state.^{15,35,55,56} As a function of θ , Figure 7 (upper part) displays the various contributions to the relative potential energy. The figure shows that electrostatics plays the primary role in the overall increase of the relative potential energy upon rotation. Detailed analysis of the pairwise contributions relative to the zero-degree system shows that the electrostatic contributions from the basal oxygen-basal silicon, ion-basal oxygen, and water-water interactions contribute to the overall increase in the relative potential energy. Hence, the electrostatic contribution due to the water network is less stabilizing for rotated than nonrotated clay layers (Supporting Information Figure S2).

As a function of θ , Figure 10a displays the density profiles of the sodium ions and water molecules (the profile does not distinguish individual atoms in the molecules) in the interlayer for the 6-0 composition. The density profile of water develops a maximum at the interlayer center with a low shoulder caused by coordination of water molecules to the clay layer edges. The density profile of the sodium ions is characterized by two peaks that occur close to the interlayer center. Interestingly, beginning with the $\theta = 3^\circ$ system, the profiles develop more pronounced peaks relative to $\theta = 0^\circ$. This indicates that upon rotation, ions are driven away from the interlayer center toward the basal planes. The process might be related to the less stabilizing impact of water-water electrostatics to the potential energy of the rotated systems.

Figure 10b shows the 2D density maps of the ions and water molecules for the 6-0 composition. Examination of Figures 1, 10b, and Supporting Information S3 (given for $\theta = 0^\circ$) shows that the H_2O molecules and sodium ions create patterns reminiscent of the Moire patterns for nonzero θ values. This striking feature indicates that rotational disordering

affects the structural arrangement of the interlayer species for hydrated montmorillonite. Similar results are obtained from analysis of the simulation data for Ca-MMT. The density distribution map also demonstrates that the ions actively explore the interlayer space in the XY planes parallel to the clay surfaces. This is distinctly different from the distribution of the ions at the 0-0 composition that revealed sharp localization in the XY plane (Figure 6b). This is a consequence of the fact that solvation by water molecules provides greater ion mobility in the interior.

In the simulations of Na-MMT with the 6-0 composition using enforced rotation, the energy and d_{001} spacing are higher for rotated structures than for the system with $\theta = 0^\circ$ (not shown). The energy curve reaches a plateau and stays relatively constant during the rotation starting from $\theta > 2 - 3^\circ$.

So far, we have considered the hydrated clay systems with water monolayer exposed to the Moire. patterns of clay sheets. Supporting Information Figure S4 shows the potential energy changes as a function of θ computed using both the position constraining and enforced rotation methods for the Na-MMT with the 14-0 composition. This composition produces a bilayer configuration of water molecules (as confirmed by the density profile) in the interlayer with the equilibrated $d_{001} - spacing$ equal to $14.67 \pm 0.03 \text{ \AA}$, the value that falls into the experimentally determined 2W hydration state range ($14.5-15.5 \text{ \AA}$)¹³ and close to the calculated stable hydration state.^{15,35,55} In this case, both methods predict that rotation from $\theta = 0^\circ$ is an endothermic process accompanied by the increase in the d_{001} -spacing. The density profiles (not shown) support the preferential location of the sodium ions near the center of the interlayer space and their solvation by water molecules. This is in line with the recent DFT-based molecular dynamics and Monte Carlo simulations of optimal ion positions in the interlayer space of hydrated montmorillonite.⁵⁷ In contrast to the system with the 6-0 composition, the calculated density maps indicate that ion distribution is relatively unaffected by the Moire pattern; the same is true for the water molecules, although they develop a cage-like pattern owing to the presence of an adjacent basal surface (Supporting

Information Figures S5.S7). The pictures provide the distribution maps computed for the ions and separately for water layers in a bilayer configuration at $\theta = 6^\circ$ as an example (the distributions for the other angles are similar). Thus, the Moire pattern exerts little influence on the distribution of the interlayer species for clay expanded into the 2W (and presumably also higher) hydration state.

Rotation of Clay Systems with Intercalated CO_2

As seen from Figures 4 and 5 the potential energy of the clay systems with 0-2 composition undergoes a slight increase as θ increases from 0° to 3° , then decreases for higher rotational angles relative to the 0° case. The corresponding d_{001} -spacing experiences a marginal expansion upon rotation. Under experimental conditions, intercalation of carbon dioxide requires a residual amount of water present in the interlayer space.^{5,10,11} The 0-2 composition considered here is an idealized system not likely observable experimentally. In contrast to this, rotation of the clay system with the 5-2 composition is accompanied by an increase in both the potential energy and the d_{001} -spacing (Figures 4 and 5).

Figure 11a and b depicts the density profiles for Na^+ ions and carbon dioxide molecules and density distribution maps for carbon dioxide molecules in Na-MMT with the 0-2 composition. The resulting profiles of the sodium ions are reminiscent of those found for the 0-0 composition (Figure 6a). The density map of the Na^+ ions (not shown) is also similar to that depicted in Figure 6b. Krishnan et al.²⁴ reported a detailed analysis of the dynamics of sodium ions and carbon dioxide molecules in the interlayer space of Na-MMT. They found that the ions primarily adsorbed at the surfaces, with some ions being located in the interior. Similar results are obtained in this work and depicted in Figure 11a, showing two minor peaks near the interlayer center. The density profile of carbon dioxide displays a maximum at the middle of the interlayer (Figure 11a). Thus, carbon dioxide and the sodium ions avoid each other, consistent with previous data.^{16,24}

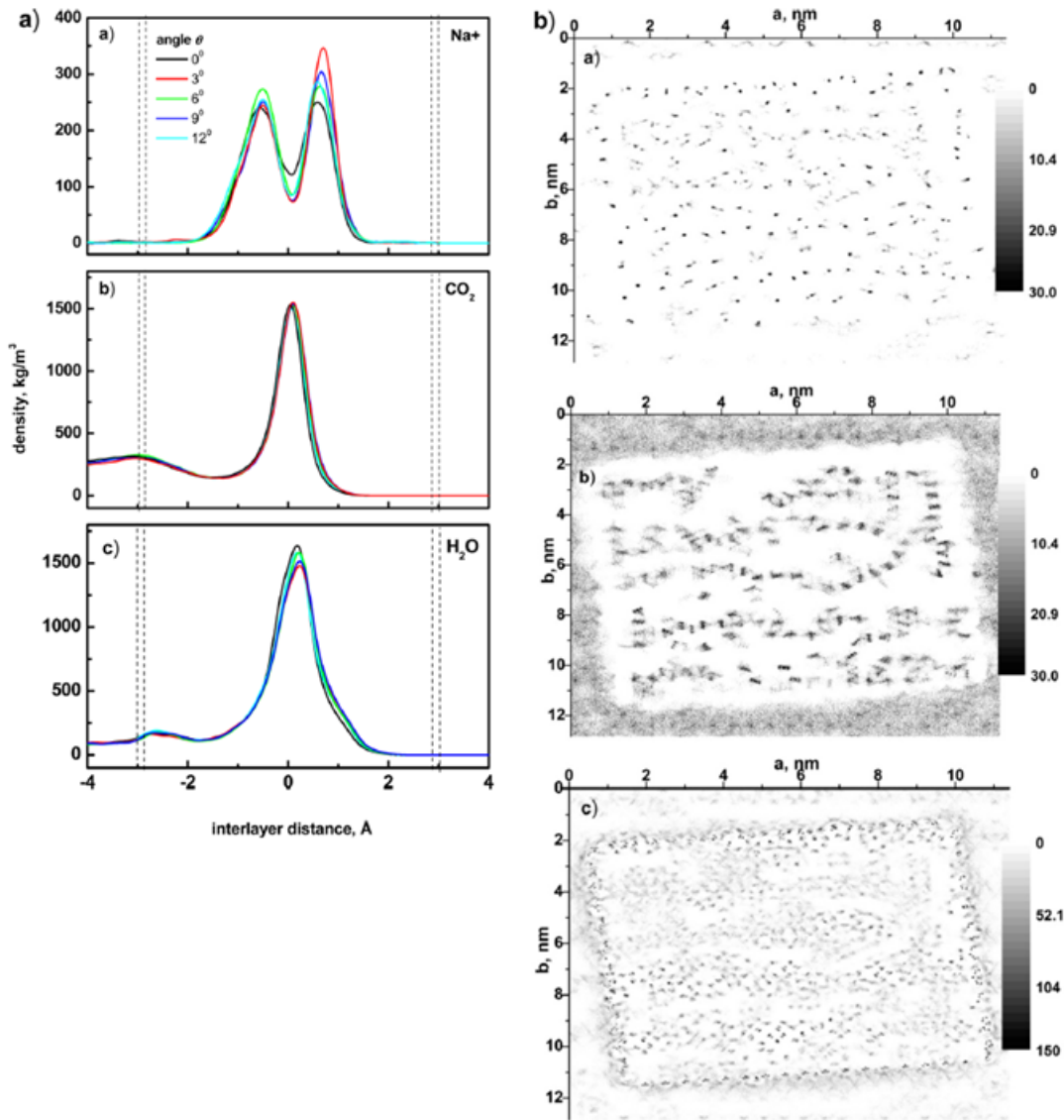


Figure 12: (a; left) Density profiles showing (a) sodium ion, (b) carbon dioxide, and (c) water molecule distributions along the distance perpendicular to the internal surfaces of Na-MMT for the 5-2 composition at various θ . Double dashed lines designate the range of positions of basal planes as a result of rotation. Profiles obtained by averaging over 20 ns of simulation time. (b; right) Density maps (density in number/ nm^3) showing (a) sodium ion, (b) carbon dioxide, and (c) water molecule distributions in the interlayer projected on a plane parallel to the internal surfaces of Na-MMT with the 5-2 composition at $\theta = 6^\circ$. Results obtained by averaging over 20 ns of simulation time.

Comparison of the density maps for the nonzero θ value (Figure 11b) and for $\theta = 0^\circ$ (Supporting Information Figure S8) has revealed that the CO_2 distribution is affected by the Moire patterns formed by the basal surfaces. However, the distribution is less structured,

to be recognized as the Moire pattern like that depicted in Figure 10b for water molecules. Similar trends were found for the Ca-MMT system.

Figure 12 reports the density profiles at various θ values and density distribution maps of the interlayer species for the 5-2 composition of Na-MMT. The sodium ion profile displays two peaks located in the interior of the interlayer space similar to the profile for the 6-0 composition (Figure 10a), suggesting that the ions become preferentially solvated by water molecules. Moreover, in line with Figure 10a, rotation of the clay sheets causes a slight increase in the separation of the peaks in the Na^+ distribution. For the 5-2 composition, the CO_2/H_2O mixture forms a monolayer correlating with the maxima of the density profiles. At the positions of the layer edges, the carbon dioxide profile develops a distinct broad shoulder and the density profile of water demonstrates a small peak (Figure 12a). The density distribution map of carbon dioxide shows elevated density in the interstitial space and at the edges of the small layer that gives rise to the shoulder seen in the density profile.

Similarly, the density distribution map of water displays an increase in density around the layer edges, although to a much lesser extent (Figure 12b). Apparently, the 5-2 composition (and 5-1, not shown) creates a mixture with a supersaturated concentration of carbon dioxide, and during equilibration, the excess of CO_2 moves from the interlayer to the interstitial space. In our earlier work, the 5-2 composition resulted in the equilibrium d_{001} -spacing equal to $14.49 \pm 0.02 \text{ \AA}$, which falls within the range of the 2W hydration state.¹⁶ The Na-MMT model employed in that work provides exposure of the interlayer species only to the internal clay surfaces (no edge effects). In this study, because the interlayer species have access to the interstitial space and edges, the equilibrium d_{001} -spacing decreased to $12.17 \pm 0.02 \text{ \AA}$ ($\theta = 0^\circ$), close to the value for the 6-0 composition (see section 3-2). Interestingly, the carbon dioxide remaining in the interlayer region tends to agglomerate and form elongated clusters (conglomerates) separated by water molecules with a residual amount of solvated CO_2 (Figure 12b). To explore the stability of such clusters, production simulations of Na- and Ca-MMT at $\theta = 6^\circ$ were conducted up to 200 ns to monitor potential energy, d_{001} -spacing

changes, and density distribution maps. At the end of the simulations, the density distributions remain unchanged, as reported in Figure 12. Density maps of water molecules display nonuniform distributions reflecting the presence of agglomerated carbon dioxide molecules in the interlayer. There are no noticeable patterns formed by water that might be connected to the Moire patterns of basal surfaces, as found for the 6-0 composition (Figure 12b). The hydrogen bonding between the interlayer species and the basal oxygens affects the energetic properties of clay systems. In this regard, it is instructive to explore hydrogen bond lifetimes as a function of interlayer composition and θ . To accomplish this, the approach described in ref⁵⁸ was engaged.

The analysis of the calculated hydrogen-bond lifetimes for water-clay, water-water, and water-carbon dioxide pairs in Na- and Ca-MMT at different θ values shows that the rotational disordering does not significantly impact the H-bond lifetimes. The water-water and water-basal oxygen hydrogen lifetimes computed for the 6-0 and 5-2 compositions have comparable values (the water-carbon dioxide values are an order of magnitude smaller, consistent with our previous results).¹⁶ This means that in the interlayer, the water molecules are strongly engaged in interactions with the basal surfaces. On the other hand, in the open environment, the H-bonding of water to a single smectite surface is weaker than H-bonds between water molecules.⁵⁹⁻⁶¹ The simulations of Na-MMT systems for the 0-2 and 5-2 compositions using the enforced rotation approach demonstrate a rise in the relative potential energy (and d_{001} -spacing) upon rotation (not shown). The energy increases even for the 0-2 composition that is found to demonstrate the opposite trend using the position restraint approach. This is attributed to nonequilibrium configurations of the interlayer species during enforced rotation. Specifically, deviation of the clay layers from $\theta = 0^\circ$ induces an increase in the potential energy of the system. To provide smoother rotation motion, the angular speed was decreased by an order of magnitude to $0.001^\circ/\text{ps}$. However, it did not reverse the trend, meaning that the 0-2 system is more sensitive to equilibration of the interlayer species than the 0-0 system, which displays a decrease in the energy and the interlayer distance at the

small θ values ($0-2^\circ$) (Figure 9).

In the discussion above, it was assumed that interlayer species possess the ability to leave the interlayer and enter the interstitial space between clay particles. This is possible if clay generally exists as particles of a limited size and thickness. In the series of works by Nadeau et al.^{62,63} it was found using XRD and TEM measurements that naturally occurring interstratified illite-smectite and chlorite-smectite and pure smectite are mixtures of thin particles of finite sizes rather than a continuous crystal phase. Interestingly, the samples of illite-smectite and chlorite-smectite display rotational turbostratic electron diffraction patterns, presumably as a consequence of clay particle agglomerates.^{62,63} For Wyoming montmorillonite, the samples show a predominance of clay particles a few thousand angstroms in size but only 10-20 Å thick. A mobile phase migrating through a geological formation enriched with swelling clays can fill the interstitial space between the clay particles and, thus, be exposed to external mineral interfaces.

Carbon dioxide molecules can become trapped in the interlayer in amounts exceeding an expected CO_2 solubility at the prevailing P-T conditions. It has been shown experimentally that exposure of dry $scCO_2$ to montmorillonite in the $> 2W$ hydration state may result in a collapse of the d-spacing to that of the 1W state.^{4,5} During that process, a portion of the water molecules leaving the interlayer can be substituted with carbon dioxide molecules. A significant portion of (wet) $scCO_2$ might remain in the interstitial region between clay particles. Recently, MD simulations were used to study the exchange of water and counterbalancing ions between the micropores and clay interlayers in Na-montmorillonite with open [010] edges.⁶⁴ It was found that for water content at the 2W hydration state, the exchange proceeds practically without a barrier for water and the ions. Energy barriers for exchange of carbon dioxide, water, and ions between the interlayer and (wet) $scCO_2$ in the interstitial space and pores are unknown. A study aiming at an estimation of those barriers would be a valuable addition to our understanding of the mechanism of carbon dioxide interaction with swelling clay minerals.

Another scenario involves intercalation of CO_2 during expansion of swelling clay minerals that might be at fractional hydration states^{53,65,66} (although it is generally believed that smectite samples exist as a set of "quantized" hydration states, i.e., (0W, 1W, 2W, 3W))^{48,67,68} Experimentally, it was found that a residual amount of water is required for successful intercalation of CO_2 in the interlayer space that expands until the d_{001} -spacing corresponds to that of the 1W hydration state.^{11,14} Interaction of Na- and Ca-exchanged-MMT samples at the 2W hydration state with variably wet $scCO_2$ can lead to swelling to the d_{001} -spacing equal to the 3W state.^{4,5} As mentioned in the Introduction, the largest expansion occurs for MMT samples at a sub-1W hydration state and is accompanied by an increase in the d_{001} -spacing from 11.3 to 12.3 Å after exposure to gaseous CO_2 ¹¹ or to 12.1 Å after interaction with anhydrous $scCO_2$.^{4,5}

The formation of CO_2 conglomerates trapped in the interlayer is supported by Schaefer et al.⁵ and Rother et al.,⁷ who indicated that CO_2 does not displace H_2O when entering the sub-1W interlayer but "rather makes room by pushing the structural units apart", and by simulation data of Yong and Smith,⁶⁹ who reported the interlayer of Sr-MMT showing water molecules clustering around the ions and away from substitutions in the octahedral layer and formation of unoccupied regions. That unoccupied space might be filled in by another species such as carbon dioxide in a two-step mechanism ("prop and fill") implying the existence of (meta)stable partially filled hydration states. In our work, we found conglomerate formations for both Na- and Ca-MMT clay systems, suggesting that CO_2 can be a filler to stabilize swelling clays during expansion. It is also important to realize that hydration energies of interlayer ions, isomorphic substitutions in octahedral, and especially tetrahedral layers would be leading factors determining trapping of CO_2 as conglomerates in smectite minerals. In the models employed in this work, only substitutions in the octahedral layer were made, so the interlayer species exposed to the basal surface were indirectly affected by charge imbalance brought by the magnesium for aluminum substitutions.

Conclusions

This study has shown that rotational disordering, a common naturally occurring phenomenon, affects the distribution of ions, water, and carbon dioxide molecules in the interlayer of swelling clays. The computed density maps reveal that the interlayer species in a monolayer configuration follow the rotational Moire patterns formed by the basal surfaces of adjacent clay layers. The simulations indicate that rotational disordering of hydrated montmorillonite and montmorillonite with intercalated water and carbon dioxide is an energetically demanding process, as found using the position constraining and enforced rotation approaches for $\theta = 0-12^\circ$. For all compositions considered, the potential energy demonstrates a tendency to reach a plateau for $\theta = 6-12^\circ$ that is attributed to a fixed number of undistorted/distorted cavities for Moire patterns. Turbostratically stacked clay layers with intercalated water and water/ CO_2 also experienced expansion of interlayer space by 0.1-0.2 Å, depending on the nature of interlayer ions.

Turbostratic dry and nearly dry montmorillonite systems are predicted to be more stable than the nonrotated system. Rotation is accompanied by a decrease in the d_{001} -spacing by ~ 0.1 Å. This process is explained in terms of favorable interactions of interlayer ions adsorbed at the clay surfaces. During equilibration, the ions find optimal positions in the interlayer, causing a decrease in the potential energy and the d_{001} -spacing. In a geological formation, this process may be anticipated during slow dehydration of expandable clays under geomechanical stress. Under such conditions, the clay layers would be prone to rotational disorder and to become turbostatically stacked in the presence of external forces shifting the clay particles. The calculation using enforced rotation of clay layers shows that perfectly oriented dehydrated montmorillonite has only a limited range ($\theta = 0-2^\circ$) for rotational disordering, and further rotation would be energetically restricted.

The results of the simulations have also shown that CO_2 might be trapped in the interlayer of hydrated montmorillonite in an amount exceeding its solubility in water at prevailing P-T conditions in subsurface geological formations. This is possible because carbon dioxide

conglomerates become trapped in the interlayer and are surrounded by water molecules with solvated CO_2 . Thus, the expandable clay layers provide a confining environment for such carbon dioxide retention. This trapping mechanism could be important in estimations of a storage capacity for selected geological sites.

Supporting Information

Eight figures describing potential energy change, electrostatic contributions of various atom pairs, 2D density maps, relative potential energy and d_{001} spacing change in Na-MMT systems. This material is available free of charge via the Internet at <http://pubs.acs.org>.

References

- (1) Geologic Carbon Dioxide Storage, NETL. <http://www.netl.doe.gov/research/coal/carbon-storage/research-and-development/storage>, Accessed: 2014-06-30.
- (2) Allen, P. A.; Allen, J. R. *Basin analysis: principles and application, 2nd ed.*; Blackwell Publishing, 2005.
- (3) Abdou, M.; Ahmaed, H. *Petroleum Science and Technology* **2010**, *28*, 934–945.
- (4) Ilton, E. S.; Schaef, H. T.; Qafoku, O.; Rosso, K. M.; Felmy, A. R. *Environmental science & technology* **2012**, *46*, 4241–4248.
- (5) Schaef, H. T.; Ilton, E. S.; Qafoku, O.; Martin, P. F.; Felmy, A. R.; Rosso, K. M. *International Journal of Greenhouse Gas Control* **2012**, *6*, 220–229.
- (6) Kwak, J. H.; Hu, J. Z.; Turcu, R. V.; Rosso, K. M.; Ilton, E. S.; Wang, C.; Sears, J. A.; Engelhard, M. H.; Felmy, A. R.; Hoyt, D. W. *International Journal of Greenhouse Gas Control* **2011**, *5*, 1081–1092.

- (7) others,, et al. *Environmental science & technology* **2012**, *47*, 205–211.
- (8) Romanov, V. N. *International Journal of Greenhouse Gas Control* **2013**, *14*, 220–226.
- (9) Romanov, V. N.; Howard, B. H.; Lynn, R. J.; Warzinski, R. P.; Hur, T. B.; Myshakin, E. M.; Lopano, C. L.; Voora, V. K.; Al-Saidi, W. A.; Jordan, K. D.; Cygan, R. T.; Guthrie, G. D. CO₂ Interaction with Geomaterials; American Geophysical Union Fall Meeting, San Francisco, December 13–17, 2010;.
- (10) others,, et al. *Langmuir* **2012**, *28*, 7125–7128.
- (11) Giesting, P.; Guggenheim, S.; Koster van Groos, A. F.; Busch, A. *International Journal of Greenhouse Gas Control* **2012**, *8*, 73–81.
- (12) Hur, T.-B.; Baltrus, J. P.; Howard, B. H.; Harbert, W. P.; Romanov, V. N. *International Journal of Greenhouse Gas Control* **2013**, *13*, 149–155.
- (13) others,, et al. *Clays and Clay Minerals* **1990**, *38*, 485–492.
- (14) Giesting, P.; Guggenheim, S.; Koster van Groos, A. F.; Busch, A. *Environmental science & technology* **2012**, *46*, 5623–5630.
- (15) Marry, V.; Turq, P.; Cartailier, T.; Levesque, D. *The Journal of chemical physics* **2002**, *117*, 3454–3463.
- (16) Myshakin, E. M.; Saidi, W. A.; Romanov, V. N.; Cygan, R. T.; Jordan, K. D. *The Journal of Physical Chemistry C* **2013**, *117*, 11028–11039.
- (17) Botan, A.; Rotenberg, B.; Marry, V.; Turq, P.; Noetinger, B. *The Journal of Physical Chemistry C* **2010**, *114*, 14962–14969.
- (18) Smith, D. E. *Langmuir* **1998**, *14*, 5959–5967.
- (19) Berendsen, H.; Postma, J.; van Gunsteren, W.; Hermans, J. *There is no corresponding record for this reference* 331–342.

- (20) Harris, J. G.; Yung, K. H. *The Journal of Physical Chemistry* **1995**, *99*, 12021–12024.
- (21) Yang, X.; Zhang, C. *Chemical physics letters* **2005**, *407*, 427–432.
- (22) Peng, X.; Zhao, J.; Cao, D. *Journal of colloid and interface science* **2007**, *310*, 391–401.
- (23) Cole, D. R.; Chialvo, A. A.; Rother, G.; Vlcek, L.; Cummings, P. T. *Philosophical Magazine* **2010**, *90*, 2339–2363.
- (24) Krishnan, M.; Saharay, M.; Kirkpatrick, R. J. *The Journal of Physical Chemistry C* **2013**, *117*, 20592–20609.
- (25) Hamm, L. M.; Bourg, I. C.; Wallace, A. F.; Rotenberg, B. *Reviews in Mineralogy and Geochemistry* **2013**, *77*, 189–228.
- (26) Guthrie, G.; Reynolds, R. *The Canadian Mineralogist* **1998**, *36*, 1421–1434.
- (27) Viani, A.; Gualtieri, A. F.; Artioli, G. *American Mineralogist* **2002**, *87*, 966–975.
- (28) Lutterotti, L.; Voltolini, M.; Wenk, H.-R.; Bandyopadhyay, K.; Vanorio, T. *American Mineralogist* **2010**, *95*, 98–103.
- (29) Moore, D. M.; Reynolds, R. C. *X-ray Diffraction and the Identification and Analysis of Clay Minerals*; Oxford university press Oxford, 1989; Vol. 378.
- (30) Veblen, D. R.; Guthrie, G. D.; Livi, K. J.; Reynolds, R. C. *Clays and Clay Minerals* **1990**, *38*, 1–13.
- (31) Güven, N. *Science* **1973**, *181*, 1049–1051.
- (32) Mering, J. *Clays and Clay Minerals* **1967**, *15*, 3–25.
- (33) Reynolds, R. *Clays and Clay Minerals* **1992**, *40*, 387–387.
- (34) D. van der Spoel, B. H., E. Lindahl; the GROMACS development team, GROMACS User Manual version 4.6.5, www.gromacs.org. 2013; <http://www.gromacs.org>.

- (35) Cygan, R. T.; Liang, J. J.; Kalinichev, A. G. *J. Phys. Chem. B* **2004**, *108*, 1255–.
- (36) Cygan, R. T.; Romanov, V. N.; Myshakin, E. M. *The Journal of Physical Chemistry C* **2012**, *116*, 13079–13091.
- (37) Allen, M. P.; Tildesley, D. J. *Computer Simulation of Liquids*; 1989; pp –.
- (38) Vlcek, L.; Chialvo, A. A.; Cole, D. R. *The Journal of Physical Chemistry B* **2011**, *115*, 8775–8784.
- (39) Van Gunsteren, W.; Berendsen, H. *Molecular Simulation* **1988**, *1*, 173–185.
- (40) Berendsen, H. J.; Postma, J. P. M.; van Gunsteren, W. F.; DiNola, A.; Haak, J. *The Journal of chemical physics* **1984**, *81*, 3684–3690.
- (41) Parrinello, M.; Rahman, A. *Journal of Applied physics* **1981**, *52*, 7182–7190.
- (42) Nosé, S.; Klein, M. *Molecular Physics* **1983**, *50*, 1055–1076.
- (43) Nosé, S. *Molecular physics* **1984**, *52*, 255–268.
- (44) Hoover, W. G. *Physical Review A* **1985**, *31*, 1695.
- (45) Tsipursky, S. I.; Drits, V. *Clay Minerals* **1984**, *19*, 177–193.
- (46) Kutzner, C.; Czub, J.; Grubmu?ller, H. *Journal of chemical theory and computation* **2011**, *7*, 1381–1393.
- (47) Voora, V. K.; Al-Saidi, W. A.; Jordan, K. D. *J. Phys. Chem. A* **2011**, *115*, 9695–.
- (48) Ferrage, E.; Lanson, B.; Sakharov, B. A.; Drits, V. A. *American Mineralogist* **2005**, *90*, 1358–1374.
- (49) Abramova, E.; Lapidés, I.; Yariv, S. *Journal of Thermal Analysis and Calorimetry* **2007**, *90*, 99–106.

- (50) Morodome, S.; Kawamura, K. *Clays and Clay Minerals* **2011**, *59*, 165–175.
- (51) Boek, E.; Coveney, P.; Skipper, N. *Langmuir* **1995**, *11*, 4629–4631.
- (52) Tambach, T. J.; Bolhuis, P. G.; Smit, B. *Angew. Chem., Int. Ed.* **2004**, *43*, 2650–.
- (53) Morrow, C. P.; Yazaydin, A. O.; Krishnan, M.; Bowers, G. M.; Kalinichev, A. G.; Kirkpatrick, R. J. *The Journal of Physical Chemistry C* **2013**, *117*, 5172–5187.
- (54) Jinhong, Z.; Xiancai, L.; Jianxi, Z.; Xiandong, L.; Jingming, W.; Qing, Z.; Peng, Y.; Hongping, H. *The Journal of Physical Chemistry C* **2012**, *116*, 13071–13078.
- (55) Whitley, H. D.; Smith, D. E. *The Journal of chemical physics* **2004**, *120*, 5387–5395.
- (56) Smith, D. E.; Wang, Y.; Whitley, H. D. *Fluid phase equilibria* **2004**, *222*, 189–194.
- (57) Suter, J. L.; Sprik, M.; Boek, E. S. *Geochimica et Cosmochimica Acta* **2012**, *91*, 109–119.
- (58) van der Spoel, D.; van Maaren, P. J.; Larsson, P.; Timneanu, N. *The Journal of Physical Chemistry B* **2006**, *110*, 4393–4398.
- (59) Zhang, G.; Al-Saidi, W. A.; Myshakin, E. M.; Jordan, K. D. *J. Phys. Chem. C* **2012**, *116*, 17134–17141.
- (60) Rotenberg, B.; Patel, A. J.; Chandler, D. *Journal of the American Chemical Society* **2011**, *133*, 20521–20527.
- (61) Marry, V.; Rotenberg, B.; Turq, P. *Physical Chemistry Chemical Physics* **2008**, *10*, 4802–4813.
- (62) Nadeau, P.; Wilson, M.; McHardy, W.; Tait, J. *Science* **1984**, *225*, 923–925.
- (63) Nadeau, P. *CLAY MINER. Clay Miner.* **1985**, *20*, 499.

- (64) Rotenberg, B.; Marry, V.; Vuilleumier, R.; Malikova, N.; Simon, C.; Turq, P. *Geochimica et Cosmochimica Acta* **2007**, *71*, 5089–5101.
- (65) Tenório, R. P.; Engelsberg, M.; Fossum, J. O.; da Silva, G. J. *Langmuir* **2010**, *26*, 9703–9709.
- (66) Tambach, T. J.; Bolhuis, P. G.; Hensen, E. J.; Smit, B. *Langmuir* **2006**, *22*, 1223–1234.
- (67) Sato, T.; Watanabe, T.; Otsuka, R. *Clays and Clay Minerals* **1992**, *40*, 103–113.
- (68) Ferrage, E.; Kirk, C. A.; Cressey, G.; Cuadros, J. *American Mineralogist* **2007**, *92*, 994–1006.
- (69) Young, D. A.; Smith, D. E. *The Journal of Physical Chemistry B* **2000**, *104*, 9163–9170.